



Distinct structure-activity relationship and reaction mechanism over BaCoO₃/CeO₂ catalysts for NO direct decomposition

Running Kang^{a,b,c}, Xuehai Wang^d, Junqin Huang^{b,c}, Sufeng An^d, Lu Wang^a, Gang Wang^{d,*}, Hong Chen^e, Cuijuan Zhang^f, Feng Bin^{b,c,**}, Yongdan Li^{a,*}

^a Department of Chemical and Metallurgical Engineering, School of Chemical Engineering, Aalto University, Kemistintie 1, Espoo, P.O. Box 16100, FI-00076, Finland

^b State Key Laboratory of High-Temperature Gas Dynamics, Institute of Mechanics, Chinese Academy of Sciences, Beijing 100190, China

^c School of Engineering Science, University of Chinese Academy of Sciences, Beijing 100049, China

^d Dalian Research Institute of Petroleum and Petrochemicals, SINOPEC, Dalian 116045, China

^e School of Environmental Science & Engineering, Tianjin University, Tianjin 300072, China

^f Collaborative Innovation Center of Chemical Science and Engineering (Tianjin), Tianjin Key Laboratory of Applied Catalysis Science and Technology, State Key Laboratory of Chemical Engineering (Tianjin University), School of Chemical Engineering and Technology, Tianjin University, Tianjin 300072, China

ARTICLE INFO

Keywords:

NO direct decomposition
Perovskite
BaCoO₃
CeO₂ morphology
Reaction mechanism

ABSTRACT

The dependency on morphology is crucial for achieving highly efficient direct decomposition of NO. Herein, a BaCoO₃/CeO₂ catalyst is synthesized using CeO₂ small particles (p), spheres (s) and rods (r) as supports. The NO conversion to N₂ (NTN2) at 800 °C follows the order BaCoO₃/CeO₂-r (78.8 %) > BaCoO₃/CeO₂-s (75.9 %) > BaCoO₃/CeO₂-p (56.9 %) > BaCoO₃ (8.6 %) at a space velocity 1 g s/cm³. BaCoO₃/CeO₂-r exhibits high tolerance to O₂ and stability with conversion decreasing from 78.8 % to 74.6 %, 60.0 % and 50.0 % at 800 °C with 1, 5 and 10 vol% O₂, respectively. The high redox activity, higher active oxygen mobility and NO adsorption capability ensures its superior performance, while the high surface area (31.29 m²/g) and uniform distribution of active sites on the surface further promote the activity. The mechanism of NO direct decomposition is elucidated by *in situ* Diffuse reflectance infrared Fourier transform spectroscopy, ¹⁸O₂ isotopic transient exchange experiments and density functional theory (DFT) calculation.

1. Introduction

Nitrogen oxides (NO_x), emitted in the flue gas of the industrial furnace such as new-type dry cement production process (800 °C) and gasification cooling stack in steelmaking (750–800 °C), are extremely toxic to human health and environment via forming acid rain, photochemical smog, and ozone layer depletion [1]. Currently, several technologies have been proposed for NO_x abatement, including selective catalytic reduction (SCR) with ammonia, selective non-catalytic reduction and NO_x storage and reduction, etc. [2–8]. Among these technologies, NO direct decomposition (2NO → N₂ + O₂) has been regarded as the most appealing pathway for NO removal due to its eco-friendly and no requirement of reductants [9]. The NO direct decomposition reaction possesses thermodynamic feasibility but belongs to a slow kinetic reaction with high activation energy (~335 kJ/mol) [10]. Therefore, the development of high-performance catalyst for NO elimination and the

elucidation of the reaction mechanism are imperative.

Transition metal oxides, rare earth metal oxides, zeolites, and perovskite catalysts have been explored for NO direct decomposition [11–14]. Recently perovskite structured oxides have been investigated in many works [15]. Xu et al. reported that BaCoO₃, BaMnO₃ and BaFeO₃ perovskite catalysts achieve NO conversion to N₂ (NTN2) of 29.2 %, 28.7 % and 24.9 % at 650 °C (1 g s/cm³), respectively [16]. CeO₂, owing to its outstanding redox activity, oxygen storage-release capability and resistance to sintering, has been widely used as one catalyst component in the three-way catalyst, etc. [17,18]. The effect of BaCoO₃ content on the activity and the interaction between BaCoO₃ and CeO₂ in a sample xBaCoO₃-CeO₂ synthesized with a citric acid-nitrate one-pot method was examined in our previous work. The NTN2 of the 5 %BaCoO₃-CeO₂ sample is 70.1 % while that of BaCoO₃ is 27.2 % at 750 °C (1.5 g s/cm³) [19]. The 5 %BaCoO₃-CeO₂ sample remains NTN2 71.1 % at 800 °C in the presence of 1 vol% O₂. In BaCoO₃-CeO₂ sample,

* Corresponding authors.

** Corresponding author at: State Key Laboratory of High-Temperature Gas Dynamics, Institute of Mechanics, Chinese Academy of Sciences, Beijing 100190, China.

E-mail addresses: wanggang.fshy@sinopec.com (G. Wang), binfeng@imech.ac.cn (F. Bin), yongdan.li@aalto.fi (Y. Li).

BaCoO₃ is proved as the primary active sites to adsorb NO, while CeO₂ improves the reducibility, oxygen mobility and sintering resistance [20]. The morphology of CeO₂ was demonstrated to influence the metal active site dispersion and induce a strong metal-support interaction (MSI) with an appropriate morphology [18,21]. But the intrinsic structure-activity relationship (morphology, reaction interface, oxygen vacancy, etc.) over BaCoO₃ loading on different morphology of CeO₂ are still lacking for NO direct decomposition reaction.

For the mechanism of NO direct decomposition on the perovskite-type catalyst, Shin et al. [22] proposed that two NO molecules attack active sites and oxygen vacancies simultaneously and nitrosyl species (NO^{*}) form and adsorb on iron ion to form N₂ and O₂ over SrFeO_{3-x} catalyst. Teraoka et al. assumed that the attacking of two NO molecules in the adjacent oxide ion vacancies happens successively on a La_{0.4}Sr_{0.6}Mn_{0.8}Ni_{0.2}O₃ catalyst and the reaction follows the first-order law [23]. Chen et al. guessed that two adsorbed NO^{*} dissociate to produce N₂ firstly, and NO^{*} reacts with surface oxygen to form a NO₂ intermediate, which decomposes rapidly to produce NO and O₂ over a La_{1.6}Ba_{0.4}NiO₄ catalyst [24]. Recently, Xie et al. thought that NO adsorption on the metal site near oxygen vacancy to form N₂O^{*} and O^{*} is the rate determining step (RDS) on a BaCoO₃-CeO₂ catalyst [21]. However, so far, there is no direct evidence to elucidate its reaction mechanism for NO direct decomposition, particularly the roles of different intermediates on the perovskite-type catalysts.

Herein, a series of CeO₂ with varying morphologies, i.e., irregular CeO₂ particles (CeO₂-p), CeO₂ spheres (CeO₂-s) and CeO₂ rods (CeO₂-r), were prepared and employed as the supports in a BaCoO₃/CeO₂ catalyst. The distinct structure-activity relationships of the catalysts were identified. The nature of reaction mechanisms with/without O₂ was investigated with *in-situ* DRIFT, isotopic (¹⁸O₂) transient exchange experiment and DFT calculation. The results obtained comprehensively elucidate the effect of CeO₂ morphology on the catalytic activity.

2. Experimental

2.1. Sample preparation

The BaCoO₃/CeO₂ catalyst samples were prepared with an excess impregnation method. The irregular CeO₂ particles (CeO₂-p) were prepared with direct thermal decomposition of Ce(NO₃)₃·6H₂O at 600 °C. Both the nano-sphere (CeO₂-s) and nano-rod (CeO₂-r) ceria samples were synthesized with a hydrothermal technique and supplied by Liaoning KeLong Fine Chemical Co., LTD, China. The prescribed amounts of Ba(NO₃)₂ and Co(NO₃)₂·6H₂O were dissolved in distilled water, and suitable amount of citric acid was added to the solution. The mole ratio of Ba: Co: citric acid is 1:1:1.5. the solution was stirred continuously at 80 °C and the CeO₂ support was immersed to achieve a loading of 5 wt% BaCoO₃. The reason for choosing BaCoO₃ with a mass ratio of 5 % in all samples is that the 5 %BaCoO₃-CeO₂ catalyst exhibit the best NO decomposition activity of all catalysts with the loading content of BaCoO₃ from 3–100 wt% in our previous work [19]. Then it was dried at 110 °C for 12 h and calcined at 400 °C for 1 h and 700 °C for 5 h. The samples are referred to as BaCoO₃/CeO₂-p (BCP), BaCoO₃/CeO₂-s (BCS), and BaCoO₃/CeO₂-r (BCR). A BaCoO₃ sample was also prepared with the dissolution of Ba(NO₃)₂, Co(NO₃)₂·6 H₂O and suitable amount of citric acid in distilled water. The solution was stirred and evaporated at 80 °C to form a gel, followed by drying at 110 °C for 12 h and calcined at 400 °C for 1 h and then at 700 °C for 5 h.

2.2. Characterization

The X-ray diffraction (XRD) patterns were recorded with a X'PERT PRO MPD Alpha1 diffractometer at 40 mA and 45 kV with a Cu K_α radiation source (λ = 0.154056 nm). Raman spectrum was carried out to obtain oxygen vacancy information on DXR (American Thermo Electron) with a 532 nm laser. The specific surface area (SSA) was measured

using a BEL sorp Mini II instrument. N₂ physisorption isotherms were acquired at −196 °C after outgassing at 250 °C for 3 h under vacuum. The morphology and elemental distribution were observed with a high-resolution transmission electron microscope (HRTEM, JEM 2100F, Oxford) equipped with energy dispersive X-ray detector (EDX) mapping (Tecnai G² F20, Oxford) and a scanning electron microscope (SEM, Hitachi S-4800). X-ray photoelectron spectroscopy measurement (XPS) was carried out with a Kratos Axis Ultra DLD spectrometer. The binding energy was calibrated with the C1s peak at 284.8 eV.

H₂ temperature-programmed reduction (H₂-TPR) was performed on an Ichem700 apparatus. The sample (50 mg) was pretreated at 500 °C for 1 h under Ar flow (30 mL/min) to remove adsorbed impurities, and then cooled down to room temperature (RT). The sample was then heated from RT to 900 °C at 10 °C/min with a flow of 5 vol% H₂/Ar (30 mL/min). Temperature-programmed desorption of O₂ (O₂-TPD, Ichem700), and NO (NO-TPD-Mass spectrometer, MS, Pfeiffer Omnistar™) were done to examine the chemisorption of O₂ and NO, respectively. For O₂-TPD, the sample was pretreated at 500 °C for 1 h under Ar flow (30 mL/min) and exposed to O₂ (30 mL/min) for 1 h at RT, followed by operating from RT to 900 °C at 10 °C/min with pure Ar (30 mL/min) after purging with Ar (30 mL/min) for 0.5 h. For NO-TPD-MS, after being pretreated at 700 °C under Ar (50 mL/min) for 1 h, the sample (200 mg) was cooled to 80 °C and then adsorbed to saturation with 2 vol% NO/Ar for 1 h. The desorption gases were recorded with the MS from 80 °C to 700 °C at 10 °C/min.

In-situ Diffuse reflectance infrared Fourier transform (DRIFT) spectra were obtained with a Thermo Fisher Scientific Nicolet iS50 spectrometer. The catalyst was pretreated in helium atmosphere with a flow rate of 50 mL/min at 600 °C for 1 h and then cooled to RT. The background spectra were collected at desired temperatures during the cooling process. Afterwards, the reaction gases of 1 vol% NO/He, and 1 vol% NO+2 vol% O₂/He were switched into the *in-situ* reaction cell with 30 mL/min for 0.5 h until stability, respectively. The steady state spectra were recorded with accumulating 32 scans at 30, 200, 300, 400, 500, 550 and 600 °C, respectively. The isotopic (¹⁸O₂) exchange experiments were carried out in an *in-situ* fixed-bed reactor (i.d. = 3 mm), and the products were monitored with an online mass spectrometer (MS, Pfeiffer Omnistar™). A four-way switch valve was firstly used to switch the gas path instantaneously and retain steady continuous flow of reactant gases, as shown in Fig. S1 in the [supporting information](#). The sample (65 mg, 0.09–0.15 mm) was pretreated at 800 °C for about 20 min at the flow rate of 30 mL/min in Ar. Afterwards, the pre-mixed reactant gas (30 mL/min, 1 vol% NO/Ar) was constantly introduced into the reactor at 800 °C for 20 min and the products were monitored with the online MS. Pure Ar was used to purge at 30 mL/min for 10 min to remove the gases. Finally, the mixed reactant gas (30 mL/min, 1 vol% NO + 1 vol% ¹⁸O₂/Ar) was pulsed into the reactor at 800 °C for about 25 min to detect the isotopic products adequately. The isotopic gas (¹⁸O₂) was supplied by WUHAN NEWRADAR SPECIAL GAS Co., LTD.

The density functional theory (DFT) simulation was further performed to clarify the perovskite-support interaction and reaction pathways, and the detailed calculation method was introduced in the [supporting information](#).

2.3. Catalytic activity

The catalyst samples (0.5 g, 35–45 mesh) were placed in a fix-bed quartz tube reactor (i.d. = 6 mm). The sample was pretreated to remove the gaseous impurities on the surface at 500 °C for 0.5 h in Ar (30 mL/min) and cool down to RT. 8000 ppm NO/Ar was introduced into the reactor at atmospheric pressure with a flow rate 30 mL/min (1 g s/cm³, GHSV=5600 h^{−1}). Each temperature step was maintained for 20 min to reach steady state from 500 to 800 °C with an interval of 50 °C. The N₂ concentration was quantified online with the same MS calibrated with an internal standard method. The concentrations of NO, O₂, CO₂ and SO₂ were measured by online multicomponent analyzers (Gasboard-

300UV for NO/O₂, Gasboard-300plus for SO₂, Hubei Cubic-Ruiyi Instrument Co., Ltd. And QGS-08 for CO₂, Maihak). The oxygen tolerance of the catalyst was measured with feeding 1, 5, and 10 vol% O₂ in the 8000 ppm NO/Ar flow with a total flow rate 30 mL/min. The 5 vol% H₂O was introduced into the gas mixture by passing the gas stream through a gas saturator at 35 °C to study the effect of H₂O.

The activity is evaluated with NTN2 according to equation (1),

$$\text{NO Conversion to N}_2 = \frac{2[\text{N}_2]_{\text{out}}}{[\text{NO}]_{\text{in}}} \times 100\% \quad (1)$$

where $[\text{NO}]_{\text{in}}$ and $[\text{N}_2]_{\text{out}}$ are the inlet and outlet concentrations of NO and N₂, respectively.

The reaction rate (*r*) of NTN2 at 800 °C is calculated with equation (2),

$$r = \frac{F \cdot c \cdot X}{W_{\text{cat}}} \quad (2)$$

where *F* is the total feed flow (mol/s), *c* is NO inlet concentration (%), *X* is NTN2 (%), *W_{cat}* is the weight of catalyst (g).

3. Results

3.1. Catalytic activity

The NO direct decomposition activity of the catalyst samples at 500–850 °C is depicted in Fig. 1a. Pure CeO₂-R exhibits almost negligible activity, achieving only 7.5 % at 850 °C. Similarly, pure BaCoO₃ displays poor activity, with the highest NTN2 at 750 °C being only 12.46 %. However, the activity sharply increased after loading BaCoO₃ on CeO₂ with different morphologies, particularly on the spherical and rod-like CeO₂ samples. The NTN2 at 800 °C follows a distinct order of BCR (78.8 %) > BCS (75.9 %) > BCP (56.9 %) > BaCoO₃ (8.6 %). The activity of BCS and BCR is about 19–22 % higher than that of the BCP sample,

indicating the beneficial interaction between BaCoO₃ and CeO₂ with regular morphologies. The activity of BCR outperforms similar catalysts reported in the literature, as indicated in Table S1. The O₂ yield over BCR is also obtained, and it attains a value of 72.9 % at 800 °C. The amount of O₂ formation is always slightly less than that of N₂ at the same temperature. But if considering the formation of a small amount of NO₂, the quantities of N₂ and O₂ are nearly balanced for NO direct decomposition, which is also verified in the reference [25,26]. Hence, it seems likely that no accumulation of oxygen is anticipated on the catalyst surface. Subsequently, the NTN2 value is mainly discussed in the NO direct decomposition reaction. The intrinsic rates of the three catalysts at 800 °C are calculated and plotted in Fig. 1b. BCR exhibits the highest rate ($2.81 \times 10^{-7} \text{ mol g}_{\text{cat}}^{-1} \text{ s}^{-1}$) among the three samples.

The O₂ resistance experiment results of BCR are presented in Fig. 1(c). The NTN2 declines from 78.77 % to 74.56 %, 60 % and 50 % at 800 °C under 1, 5 and 10 vol% O₂, respectively. Furthermore, The BCR sample shows a stable performance in the presence of 5 vol% O₂ over 12 h with only about 5 % decrease in conversion, see Fig. 1(d). The period drops and variation of the activity for the 8000 ppm NO/Ar + 5 vol% O₂ of Fig. 1d may be attributed to the slight change of vacuum degree in the mass spectrometer. Then under the coexistence of 5 vol% O₂ and 5 vol% H₂O, the NTN2 is stably sustained about 43 % over 12 h after slight decreases from 52 % to 44 % within the initial 5 h. Further, the BCR catalyst experiences an evident activity reduction from 53.1 % to 37.4 % after feeding 1 vol% NO/Ar+5 vol% H₂O+100 ppm SO₂ for 10.5 h. The NTN2 of BCR catalyst decreases from 50.9 % to 40 % for 11 h under the 1 vol% NO/Ar+5 vol% CO₂ atmosphere. The negative effect of CO₂ is due to the CO₂ can strongly adsorb on the Ba sites of BCR to form carbonate, in agreement with the results in the reference [27]. Therefore, the existence of O₂, CO₂, H₂O and SO₂ in actual flue gas all impede the catalytic performance of BCR catalyst for NO direct decomposition.

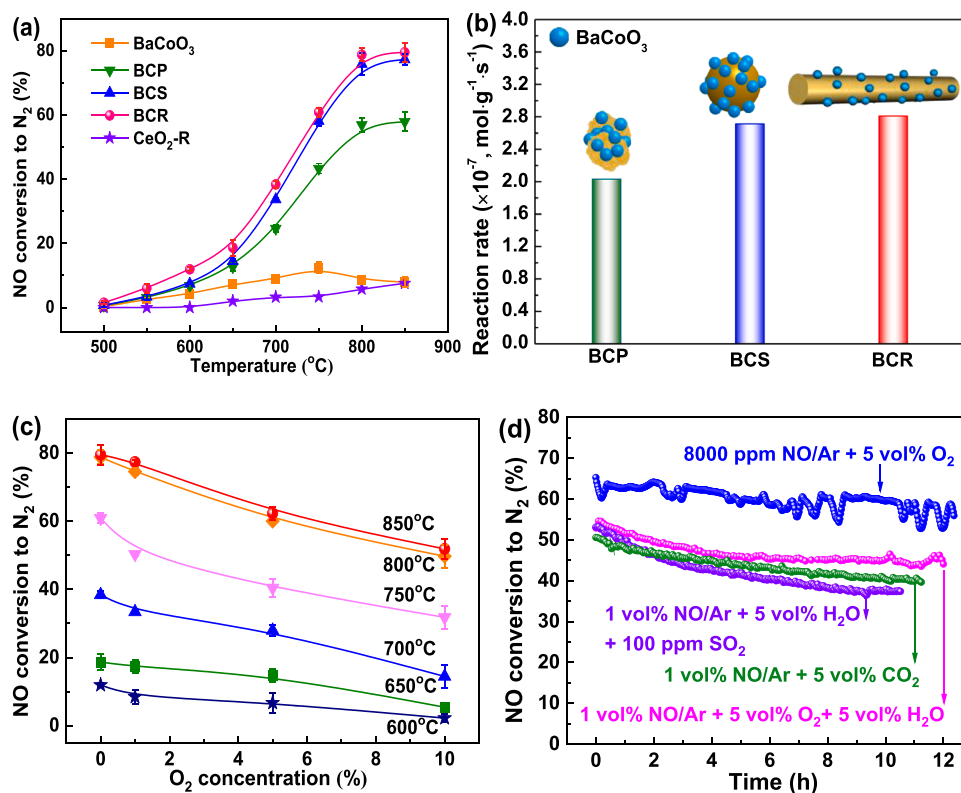


Fig. 1. (a) NO direct decomposition activity over BaCoO₃, BCP, BCS, and BCR catalysts. (b) Reaction rate of the three catalysts at 800 °C. (c) Activity of BCR with 8000 ppm NO/Ar + 1–10 vol% O₂. (d) Long-term stability at 800 °C over BCR.

3.2. Structure and texture

The XRD patterns of the catalyst samples are presented in Fig. 2. For the BaCoO₃/CeO₂ samples, only the peaks of CeO₂ phase appear and no diffraction peaks of BaCoO₃ phase are observable no matter of the CeO₂ morphology, indicating well dispersion of BaCoO₃ on CeO₂. Compared to the patterns of the pure CeO₂ samples, i.e., the p, s and r, see Fig. S3, no shift of CeO₂ peaks are observed. This result suggests that inter-diffusion may not occur between the BaCoO₃ and CeO₂ components. The BaCoO₃ sample prepared under the same condition shows an XRD pattern typically for the perovskite phase (JCPDS 70-0363). The Raman spectrum is further performed in Fig. 2(c). For the catalysts containing cerium, the peak at 458–468 cm⁻¹ belongs to the F_{2g} symmetric vibration of oxygen atoms with the fluorite-type structure cerium in CeO₂ [28,29]. Compared with pure CeO₂-r (468 cm⁻¹), the F_{2g} peaks of BCP, BCS and BCR are slightly shifted to lower wave number (458 cm⁻¹) and peaks intensity becomes weaker, attributing to the addition of BaCoO₃ causing distortion of CeO₂ lattice structure to form more oxygen vacancies, particularly for BCR. There are three additional bands at 232, 598 and 1172 cm⁻¹, owing to modes of second-order transverse acoustic (2TA), defect-induced (D), and longitudinal optical (2LO), respectively [27]. The peak at 616 cm⁻¹ is assigned to the typical vibration peak for perovskite-type structure of BaCoO₃. The oxygen vacancy (O_v) concentration (I₅₉₈/I₄₅₈) was also obtained by semiquantitative analysis in Fig. 2(d). It is clearly seen that the O_v concentration decreases with the sequence of BCR (0.13) > BCS (0.10) > BCP (0.06) > CeO₂-r (0.02). The highest O_v concentration in BCR is resulted from the stronger interface interaction between BaCoO₃ and CeO₂-r, which generates more lattice defects and oxygen vacancy.

The N₂ adsorption-desorption isotherms and pore size distribution curves of the samples are plotted in Fig. 3. All the samples exhibit type IV isotherms with a H3-type hysteresis loop, illustrating that mesopores with good pore connectivity are dominant in Fig. 3a. The SSA of the

samples follows an order of BCR (31.3 m²/g) > BCS (28.6 m²/g) > BCP (15.6 m²/g) > BaCoO₃ (1.2 m²/g), which is in consistency with the activity order. It indicates that BCR displays the highest SSA, attributed to the rod morphology of CeO₂ impedes effectively the catalyst sintering and is beneficial to promote the dispersion of active sites [28,29]. The average pore size of BCR is the smallest (15.98 nm) and the pore size distributes in the range of 2–20 nm in Fig. 3b.

Fig. 4 and S4 give the micrographs of the three catalyst samples. The particles in BCP are small agglomerates, while BCS and BCR display well-defined CeO₂ spheres and rods with large particle sizes, Fig. 4a1-c1. The average particle sizes for the BCP, BCS and BCR samples are ~27 nm, ~184 nm and ~5 μm, respectively. The HRTEM images, Fig. 4a2-c2, show that the (110), (102), (101), (211) planes of BaCoO₃ in the samples are observed, corresponding to the lattice fringes of 0.28, 0.21, 0.34 and 0.17 nm, respectively. The CeO₂ supports show *d*-spacing of 0.32 nm with (111) facets for BCP, 0.19 nm with (220) facets for BCS, and 0.19 and 0.32 nm with (220) and (111) facets for BCR. Herein, the major exposed facets are (111) for BCP, (220) for BCS and BCR, in good agreement with the literature [28,29]. Compared with (111) plane of CeO₂ for BCP, the (220) plane of CeO₂ is unstable and has lower formation energy of oxygen vacancy for BCS and BCR. Ba, Co, and Ce elements distribute evenly on all the catalyst samples surface, evidenced by the STEM-EDX mapping graphs in Fig. 4a3, b3 and c3.

3.3. Surface states and chemisorption

Fig. 5 plots the XPS Co 2p, Ce 3d and O1s spectra of the three catalyst samples in comparison with those of BaCoO₃ and CeO₂. The results of elemental analysis calculated with peak area integration are listed in Table 1. The Co 2p spectrum of pristine BaCoO₃ is deconvoluted to distinguish the Co³⁺ and Co²⁺ contributions. The peaks at 779.6 and 794.8 eV are attributed to Co³⁺ while 781.2 and 796 eV are assigned to Co²⁺ in Fig. 5a [30]. The peak position of Co³⁺ shifts to higher binding

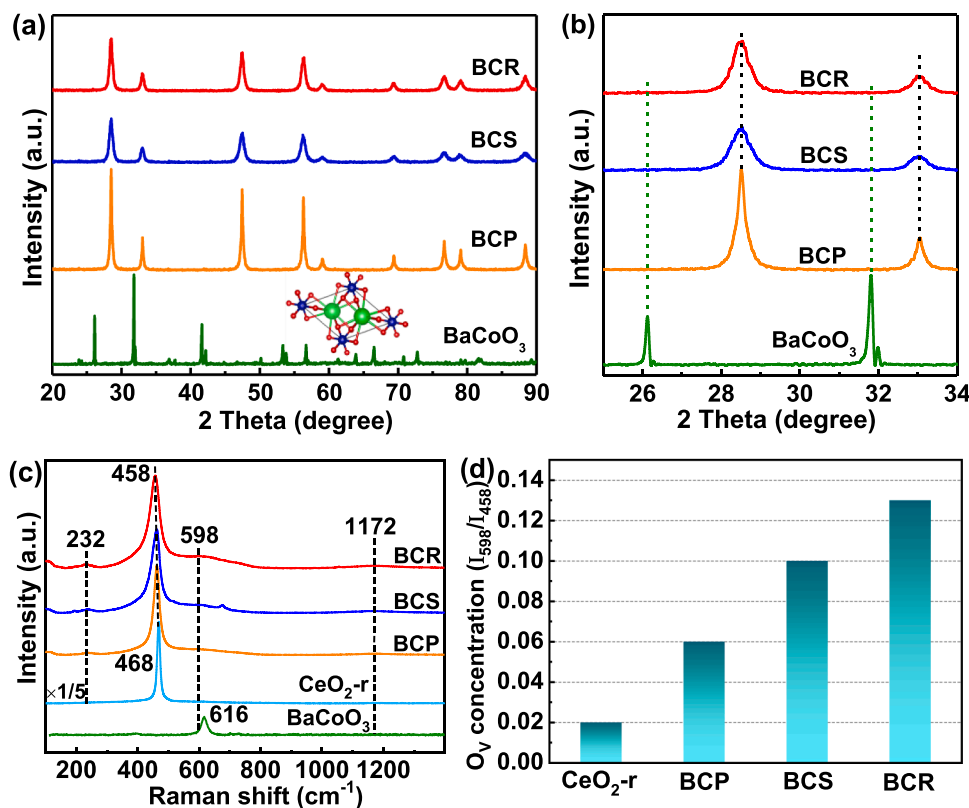


Fig. 2. (a) XRD profiles of BaCoO₃, BCP, BCS, and BCR catalysts, (b) Enlargement of the XRD profiles with the 2θ range at 25–34°, (c) Raman spectra, and (d) O_v concentration of catalysts.

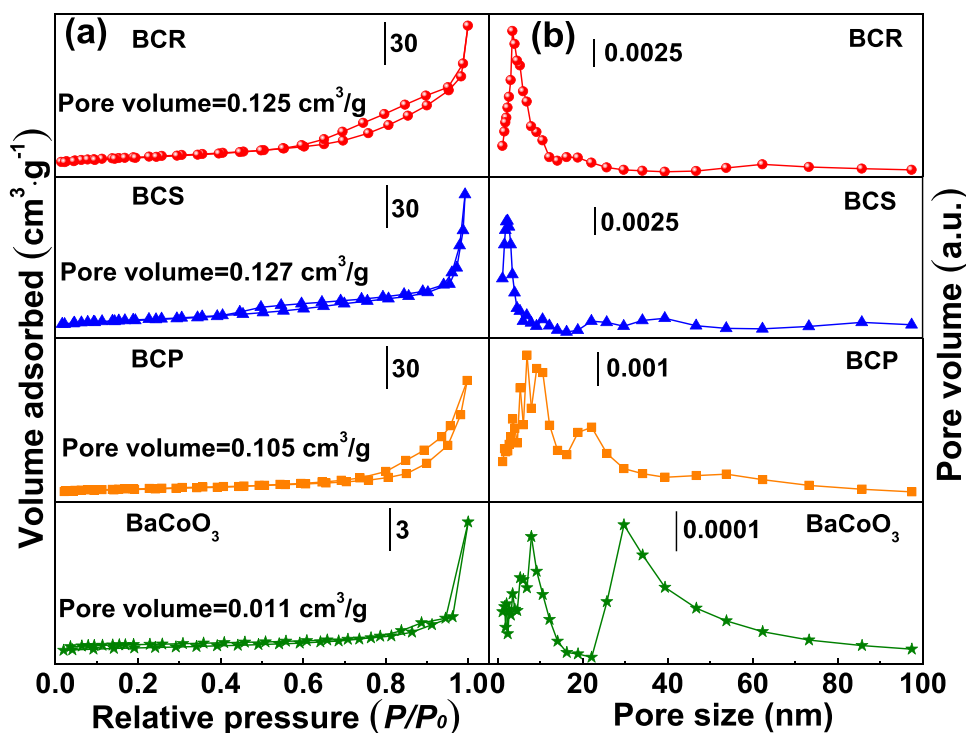


Fig. 3. (a) N_2 adsorption and desorption isotherms, and (b) pore size distributions of the $BaCoO_3$, BCP, BCS, and BCR catalysts.

energy (~ 780.5 eV) in the three catalyst samples. Meanwhile, the part of Co^{3+} transfers to Co^{2+} at 796.1 eV owing to the electron transfers of Co species on the surface of CeO_2 support during high temperature calcination step [31]. The semi-quantified Co^{3+}/Co^{2+} ratio of BCP, BCS, and BCR samples are 2.66, 3.32, and 3.58, respectively. For the Ce 3d spectra in Fig. 5b, the spectra of the three catalyst samples can be fitted to eight peaks ($u, u', u'', u''', v, v', v''$ and v'''), which are assigned to u' and v' for Ce^{3+} that favors oxygen vacancies formation, as well as u, u'', u''', v, v'' and v''' for Ce^{4+} [32]. The amount of Ce^{3+} is related to the amount of oxygen vacancies (O_v) in CeO_2 . The Ce^{3+}/Ce^{4+} ratio is calculated based on the peak areas, which decreases in the sequence of BCR (0.19) > BCS (0.18) > BCP (0.16), suggesting that relatively higher amount of Ce^{3+} and O_v exist in BCR sample. Among the three catalyst samples, the higher ratios of Co^{3+}/Co^{2+} and Ce^{3+}/Ce^{4+} in BCR induce electron transfer at the interface between $BaCoO_3$ and CeO_2 . As shown in Fig. 5 (c), the O 1s spectrum has three peaks at ~ 529.2 , ~ 531.2 and ~ 533.7 eV, corresponding to lattice oxygen (O_{lat}), adsorbed oxygen (O_{ads}) and hydroxyl oxygen (O_{OH}) species, respectively [33]. The $O_{ads}/(O_{ads}+O_{lat}+O_{OH})$ ratio has an order of BCR (0.32) > BCS (0.30) > BCP (0.29), in agreement with the ranking of Ce^{3+}/Ce^{4+} ratio in the catalysts and Raman results (Fig. 2d). The ratio of adsorbed oxygen is correlated to the oxygen vacancy concentration [34]. Thus, the BCR shows a superior activation, transformation and desorption of oxygen via the function of $Ce^{3+}-[O_v]$. Furthermore, the characteristic peaks of O_{lat} for BCP, BCS and BCR are located at lower binding energy at 530.6–530.8 eV than that for pure CeO_2 -r (531.2 eV) and $BaCoO_3$ (531.15). This observation indicates the higher mobility of lattice oxygen and formation of more oxide ion vacancies by introducing CeO_2 supports in BCP, BCS and BCR catalysts, particularly in BCR, which promotes the catalytic activity.

The pure $BaCoO_3$ shows three peaks in its H_2 -TPR profile Fig. 6(a), labeled as α_1 (362 °C), α_2 (499 °C) and α_3 (610 °C), corresponding to the reduction steps of Co^{4+} to Co^{3+} , Co^{3+} to Co^{2+} and maybe Co^{2+} to Co^0 , respectively [35,36]. For pure CeO_2 -r, two peaks at β_1 (595 °C) and β_2 (821 °C) are assigned to the reduction of surface and bulk Ce^{4+} to Ce^{3+} , respectively [37]. It is explicit that the α peak (including α_1 at 294 °C, α_2 at 340 °C and α_3 at 360 °C) for BCP, BCS and BCR catalysts shift to lower

temperatures and still mainly exist as Co^{3+} compared to those of the pure $BaCoO_3$. Meanwhile the β_1 reduction peak almost disappears in all three catalysts. Obviously, the $BaCoO_3$ component is highly dispersed on the CeO_2 surface and strong synergy between two phases, benefiting to promote the reduction activity. In addition, the actual H_2 consumption of α peak (Fig. 6d) follows order BCR (254.7 $\mu mol/g$) > BCS (217.3 $\mu mol/g$) > BCP (186.5 $\mu mol/g$). The H_2 consumption of Cerium species (β peak in Fig. 6d) is similar in these three catalysts. These mean that the more Co^{3+} species reduction and stronger interaction occurs in BCR, contributing to enhanced catalytic activity.

The mobility of lattice oxygen is examined by O_2 -TPD in Fig. 6(b). Two peaks contain adsorbed oxygen on the oxide ion vacancies (~ 730 °C) and lattice oxygen (~ 860 °C) in the catalysts [38]. Compared with the desorption peak temperature of lattice oxygen in pure $BaCoO_3$, the peaks of BCP, BCS and BCR shift to lower temperatures orderly, suggesting that different morphology of CeO_2 effectively weakens the Co-O bond strength and promotes the desorption of oxygen from $BaCoO_3$. Particularly, the BCR owns the highest lattice oxygen mobility, which is conducive to enhance activity and resistance of O_2 .

Fig. 6(c) displays the NO-TPD profiles to analysis NO sorption of catalysts. There are two NO desorption peaks at 314 and 507 °C for pure $BaCoO_3$, meanwhile NO desorbs at 256 and 525 °C for pure CeO_2 -r [39, 40], which are attributed to weak and strong NO adsorption species on different components, respectively. The BCP, BCS and BCR show similar NO desorption profiles but all bigger than that of pure samples due to the interaction effect may produce more electron coordination environment on the active sites to adsorb NO. Combined to the calculated NO desorption amount of catalysts (Fig. 6d), decreasing in the order of BCR (318.3 $\mu mol/g$) > BCS (260.3 $\mu mol/g$) > BCP (228.1 $\mu mol/g$) > $BaCoO_3$ (122.3 $\mu mol/g$) > CeO_2 -r (75.8 $\mu mol/g$). BCR exhibits the highest NO adsorption capacity and hence increase activity. Accordingly, the reducibility, mobility of lattice oxygen and NO sorption of catalysts decrease in the sequence of BCR > BCS > BCP > $BaCoO_3$, in agreement with the variation of activity results (Fig. 1a).

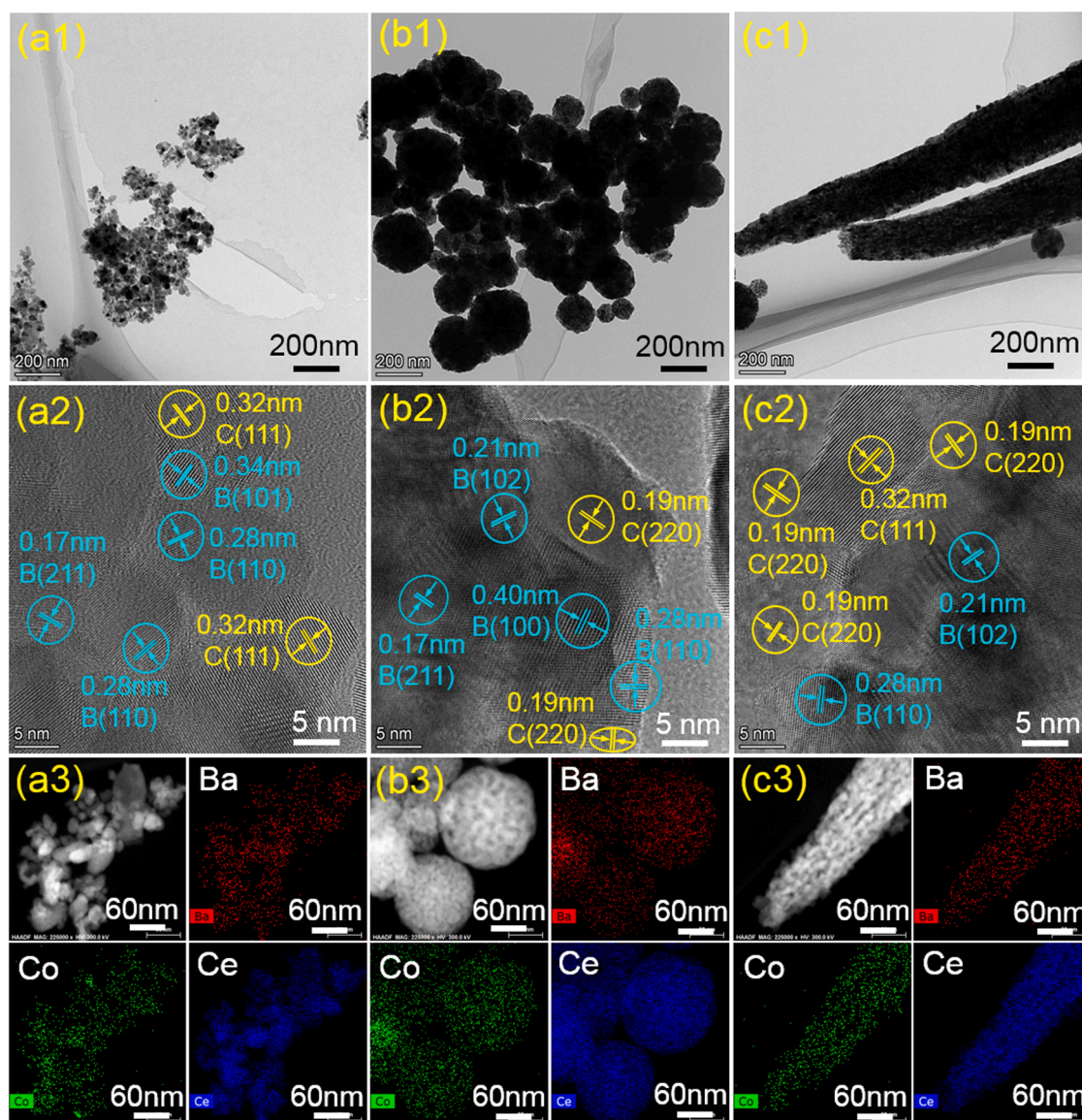


Fig. 4. TEM, HRTEM and STEM-EDX mapping for different catalysts: (a1, a2, a3) BCP, (b1, b2, b3) BCS, and (c1, c2, c3) BCR. B represents BaCoO₃, and C stands for different CeO₂ supports.

3.4. In situ DRIFT and isotopic (¹⁸O₂) tracing experiments

To further investigate the adsorbed intermediates and reaction behavior of the samples, *in-situ* DRIFT is applied with BCR sample (Fig. 7), and corresponding detailed assignment of NO adsorption bands are listed in Table 2. As shown in Fig. 7(a), the *in-situ* DRIFT profiles are recorded under 1 vol% NO/He from 30 to 600 °C. The intensity bands for nitrous oxide (N₂O) at 2240 and 2210 cm⁻¹ are weak at 30 °C and then gradually disappear with the temperature increase from 200 to 600 °C (Fig. 7b) [41]. In general, the N₂O acts as main intermediate and decomposes quickly at higher temperature and few parts of N₂O still adsorb on the catalyst surface [41]. The adsorbed mononitrosyl (NO⁺) at 1930 and 1845 cm⁻¹ are assigned to Co³⁺ sites, revealing that the cobalt species acts as the main active center for NO decomposition reaction [20,42,43]. The intensity of mononitrosyl peak becomes weaker with the temperature increase, whilst the monodentate nitrite (NO₂⁻) adsorbed on Co³⁺ (1520 cm⁻¹) becomes stronger, suggesting that the subsequent transformation from NO⁺ to NO₂⁻ on the Co species of catalyst [44]. The band at 1774 cm⁻¹ for asymmetric nitric oxide dimer ((-NO)₂/-NOON) is formed on Co²⁺ during the NO adsorption process

[20,21,45], in agreement with the IM2 structure in the following DFT results of Fig. 9(c) and (d). The intense bands of NO⁺ on Co³⁺ and weak -(NO)₂ species formed on Co²⁺ show the Co³⁺/Co²⁺ cycles supply effective electrons for the NO adsorption and transformation, in consistency with the ratio of Co³⁺/Co²⁺ in XPS results (Fig. 5a). In addition, the chelating bidentate nitrite (NO₂²⁻) adsorbed on CeO₂ (1238 and 813 cm⁻¹) turns weaker, probably due to NO₂²⁻ desorbs in the form of NO₂ molecule at the certain temperature [46]. The strong bands at 1608–1013 cm⁻¹ are attributed to the nitrate species with different adsorption states [26,47]. Those adsorption species become more stable and stronger with the temperature increase to 200 °C, particularly nitrate free ion to 400 °C, and then decompose at the higher temperature with the decreased band intensity until almost disappear at 600 °C. The contribution of Ba is more likely to promote the reduction of Co ions and formation of oxygen vacancy for stable ABO₃ perovskite type catalyst [24].

The effect of O₂ on the adsorbed intermediate species over the BCR was also explored under 1 vol% NO+2 vol% O₂/He in Fig. 7(c) and (d). The intensity of bridging bidentate nitrate (1608 cm⁻¹) and monodentate nitrate (1408 cm⁻¹) become stronger than that of 1 vol% NO/

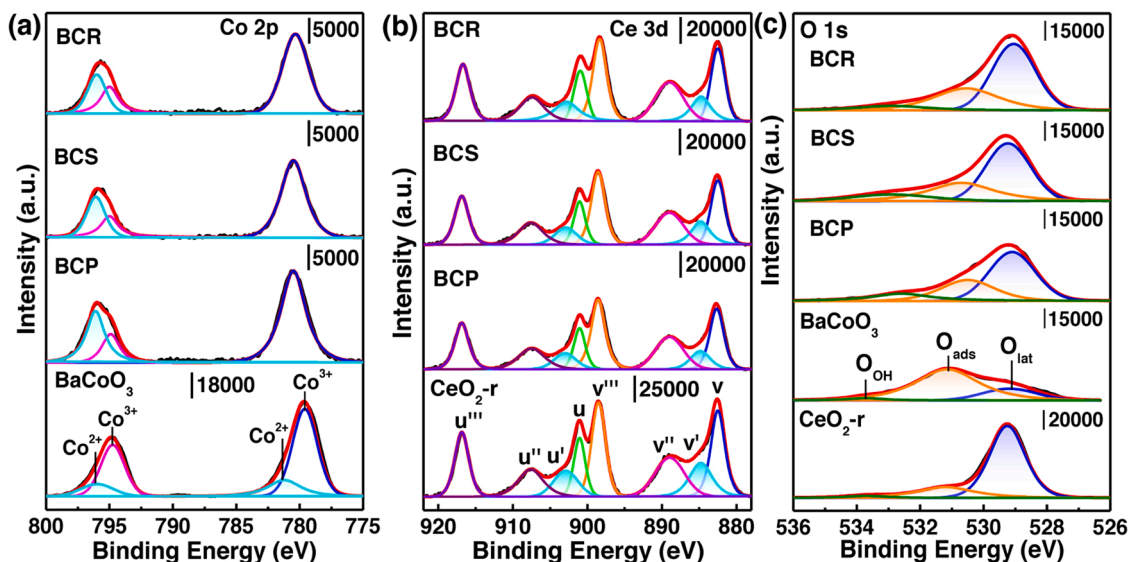


Fig. 5. XPS spectra of catalysts (a) Co 2p (b) Ce 3d, and (c) O 1s for BaCoO₃, CeO₂-r, BCP, BCS, and BCR catalysts.

Table 1

Surface atomic ratios of catalysts obtained by XPS semi-quantitative analysis.

Catalysts	Surface area ratio		
	Co ³⁺ /Co ²⁺	Ce ³⁺ /Ce ⁴⁺	O _{ads} /(O _{ads} +O _{lat} +O _{OH})
CeO ₂ -r	–	0.23	0.21
BaCoO ₃	2.69	–	0.75
BCP	2.66	0.16	0.29
BCS	3.32	0.18	0.30
BCR	3.58	0.19	0.32

He condition, and even maintain at 600 °C although the similar variation occurs for other peaks. It infers that the O₂ facilitates the formation of stable nitrate species on the surface, restraining the activity of catalyst in some extent [48]. Notably, the intensity of adsorbed NO on Co species, N₂O and nitrite species is similar under both conditions, which evidences that the Co species acts as main active center, and the active intermediate species are N₂O and nitrite instead of nitrate species. The addition of CeO₂ support effectively protects Co species from O₂ atmosphere.

The isotopically labeled ¹⁸O₂ gas as reactant in steady-state is used to further distinguish the intrinsic effect with/without O₂ for NO direct decomposition, as shown in Fig. 8. Firstly, the blank calibration without catalyst at room temperature was performed in the reactor to clarify the actual components of reactant gases (Fig. 8a). The standard transient response curves of NO and ¹⁸O₂ were detected after introducing the mixed gases (1 vol% NO + 1 vol% ¹⁸O₂/Ar). Both NO and ¹⁸O₂ signals increase sharply and simultaneously at the beginning of mixed gases feeding to the reactor, which quickly produces response signals of gases. Then NO and ¹⁸O₂ curves keep stable and other gas signals (N₂, ¹⁶O₂ and ¹⁶O¹⁸O) were not monitored, indicating that no other impurity gas existed in the mixed reactant gases. The pure Ar (30 mL/min) was purged to remove reactants existed in the reactor after realizing steady state of each reaction stage. The effect of O₂ on the NO direct decomposition was illustrated in Fig. 8(b). Before the reaction, the fresh BCR was pretreated and kept in Ar (30 mL/min) at 800 °C. The evident and stable signals of N₂ and ¹⁶O₂ can be observed owing to the NO efficient decomposition at 800 °C over the BCR catalyst after switching 1 vol% NO/Ar, while no by-product forms (Fig. S5). Then the mixed gas of 1 vol% NO + 1 vol% ¹⁸O₂/Ar was fed to the reactor after purging with pure Ar. It is noted that the three different O₂ isotopomer products (¹⁶O₂, ¹⁶O¹⁸O and ¹⁸O₂) were detected in turn. Firstly, large amounts of ¹⁶O₂

produced quickly, which decreased rapidly and then increased gradually to steady value with increasing reaction time, attributed to NO decomposition product and releasing from the BCR itself. The heteroexchange of ¹⁸O₂ with original ¹⁶O in catalyst was noticed at high temperature with high oxygen mobility [49]. After ¹⁶O₂ desorption from catalyst, the oxygen vacancy sites generated accordingly are simultaneously replenished by the surface adsorption and dissociation of gaseous ¹⁸O₂ molecules followed by the lattice oxygen diffusion, resulting in the ¹⁶O₂ signal produced quickly and then decreased [50]. The N¹⁸O should be considered to produce because of the same *m/z* (32) to ¹⁶O₂. The signal of N¹⁸O/¹⁶O₂ increased gradually to steady with increasing time reflects that the oxygen of NO can be exchanged with the part of adsorbed ¹⁸O from the catalyst surface to form N¹⁸O, which is also supported by Damma et al. [51]. Subsequently, the cross-labeled ¹⁶O¹⁸O generated quickly, corresponding to the rapid decrease of ¹⁶O₂, suggesting that the suitable lattice ¹⁸O species adsorbed on the surface oxygen vacancies start to participate NO decomposition and promote ¹⁶O¹⁸O and N₂ formation, in associate with the stable N₂ signal at that time. Afterwards, the ¹⁸O₂ increased gradually and tend to reach steady state with the increase of reaction time, attributed to excess gaseous ¹⁸O₂ fills more oxygen vacancies firstly but can not exchange completely, resulting in a competitive adsorption with NO on the oxygen vacancies and the catalytic activity decreases slightly, corresponding to a gradual decrease of N₂ formation after about 60 min. It suggests that the updated and appropriate lattice oxygen (¹⁸O) species accelerate the reaction at the beginning of O₂ addition. However, excess ¹⁸O₂ produces an inhibition effect of NO adsorption and transformation. In addition, very small amounts of intermediate species (N¹⁸O, N¹⁶O¹⁸O and N¹⁶O₂) can be obtained, which may not decompose (Fig. S4). On the basis of isotopic (¹⁸O₂) tracing studies, it can be found that moderate labile oxygen species on the surface oxygen vacancies of catalyst play a key role in NO direct decomposition reaction.

3.5. DFT calculation results

To deeply understand the synergy effect between BaCoO₃ and CeO₂ support of catalyst and direct decomposition mechanism of NO, the DFT+U method is performed to study this reaction. The reaction pathway is connected by initial state (IS), intermediate (IM), transition state (TS) and final state (FS). Based on catalyst morphology of TEM and XRD, pure BaCO₃(101), BaCO₃/CeO₂ (110) for BCS and BCR, and BaCO₃/CeO₂ (111) for BCP models are constructed in Fig. 9(a). The reaction mechanisms of NO on BaCoO₃/CeO₂ (110) and BaCoO₃/CeO₂

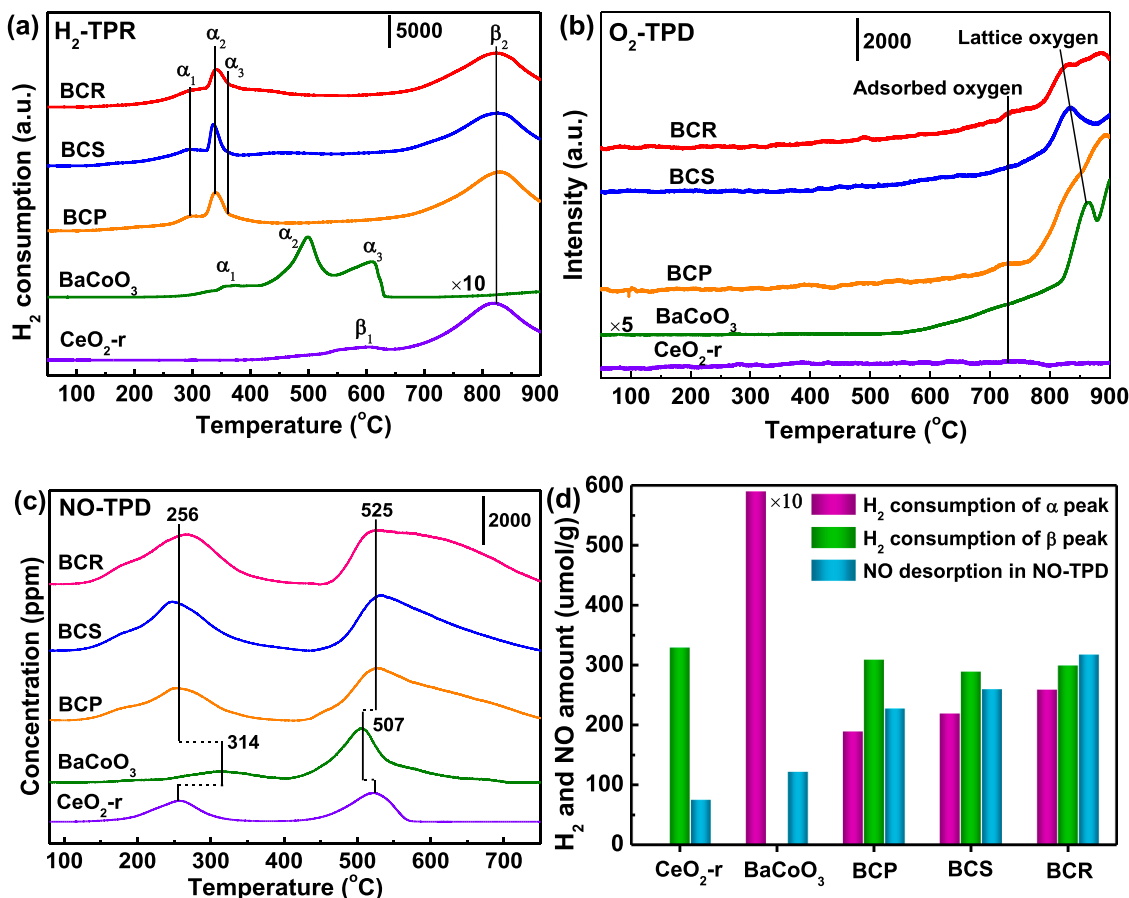


Fig. 6. (a) H₂-TPR, (b) O₂-TPD, (c) NO-TPD and (d) H₂ consumption and NO adsorption for catalysts.

(111) surfaces have been explored, as in Fig. 9. The adsorption of NO on the two different surfaces has been investigated. NO can be adsorbed on the surfaces through either the N-end or the O-end. Adsorption structures through the N-end are more stable on both BaCoO₃/CeO₂ (110) and BaCoO₃/CeO₂ (111) surfaces, with adsorption energies of 0.82 eV and 0.57 eV, respectively. Namely, NO adsorption on BaCoO₃/CeO₂ (110) releases ~ 0.25 eV more energy compared to on BaCoO₃/CeO₂ (111). On the other hand, adsorption through the O-end on the surfaces has lower energies, with values of 0.38 eV and 0.20 eV, respectively. The direct decomposition mechanism of NO on the BaCoO₃ (101) surface is also proposed in Fig. S5. Similarly, NO is also adsorbed through the N-end on the surface with the bigger adsorption energy (0.46 eV) than the O-end on the surface (0.33 eV), suggesting that the structure with NO adsorbed through the N on the surface is more advantageous on BaCoO₃. As the second NO molecule is adsorbed on the surface, the two NO molecules can directly react to form a bridging *NOON species (IM2). This reaction process releases energies of 1.72 eV for BaCoO₃/CeO₂ (110) and 1.99 eV for BaCoO₃/CeO₂ (111). Unlike on BaCoO₃ (Fig. S6), this transition state can occur spontaneously without the energy barrier on BaCoO₃/CeO₂. As the reaction progresses, the *NOON species undergoes a turnover to adsorb on the surface through the O-end (IM3). Different from that on BaCoO₃ with the negligible energy (0.08 eV), this process requires energies of 0.70 eV (BaCoO₃/CeO₂ (110)) and 1.01 eV on (BaCoO₃/CeO₂ (111)). This can be attributed to the stronger interaction between the N-end and the Co adsorption sites. Alternatively, NO can also directly form the IM3 structure through the O-end. After the second NO molecule is adsorbed through the O-end on the surface, it can directly react with the already adsorbed NO to form a *NOON species connected on the surface through the O-end. This process is also a barrierless reaction. As one of the N-O bonds in *NOON is broken (TS1), the dissociated *O atom fills an oxygen vacancy on the

surface, while *N₂O molecule adsorbs on the surface through the O-end (IM4), in agreement with *in situ* DRIFT results. The energy barrier for this process is ~ 0.6 eV. Finally, after overcoming an energy barrier of about 1 eV, the N-O bond in *N₂O is broken (TS2). The *O atom fills the vacancy, while N₂ desorbs from the surface. The reaction energies for this process are 1.11 eV for BaCoO₃/CeO₂ (110) and 1.26 eV for BaCoO₃/CeO₂ (111), respectively. In addition, the energy barrier of O₂ adsorbed on the Co site is about 0.36 eV for BaCoO₃/CeO₂ (110), which is lower than that of NO adsorbed on the Co site, suggesting the NO is easier to adsorb on active sites.

4. Discussion

4.1. Intrinsic structure-activity relationship

The intrinsic catalytic activity of the BaCoO₃/CeO₂ catalyst shows a significant morphology-dependent behavior, which is displayed in Scheme 1. The addition of CeO₂ with different morphology induces a sensitive perovskite-support interaction (PSI). BCR owns the largest average particle size (~ 5 μ m) and SSA with regular rod appearance, which provides enough reactive interface area to adsorb and transform reactants, which not only alleviates the sintering of BaCoO₃ effectively but also strengthens the synergy between BaCoO₃ and CeO₂-r (Figs. 3 and 4). Hence, the well dispersed BaCoO₃ on the surface of CeO₂ support, and both components contact with each other closely to form effective reaction interface is beneficial for strong interaction to promote activity in NO direct decomposition. Compared with (111) plane of CeO₂ for BCP, the (220) plane is unstable and has lower formation energy of oxygen vacancy for BCS and BCR. Meanwhile, the higher ratios of Co³⁺/Co²⁺, Ce³⁺/Ce⁴⁺, O_{ads}/(O_{ads}+O_{lat}+O_{OH}) and O_v concentration of the BCR sample were induced by PSI, exhibiting more active electron

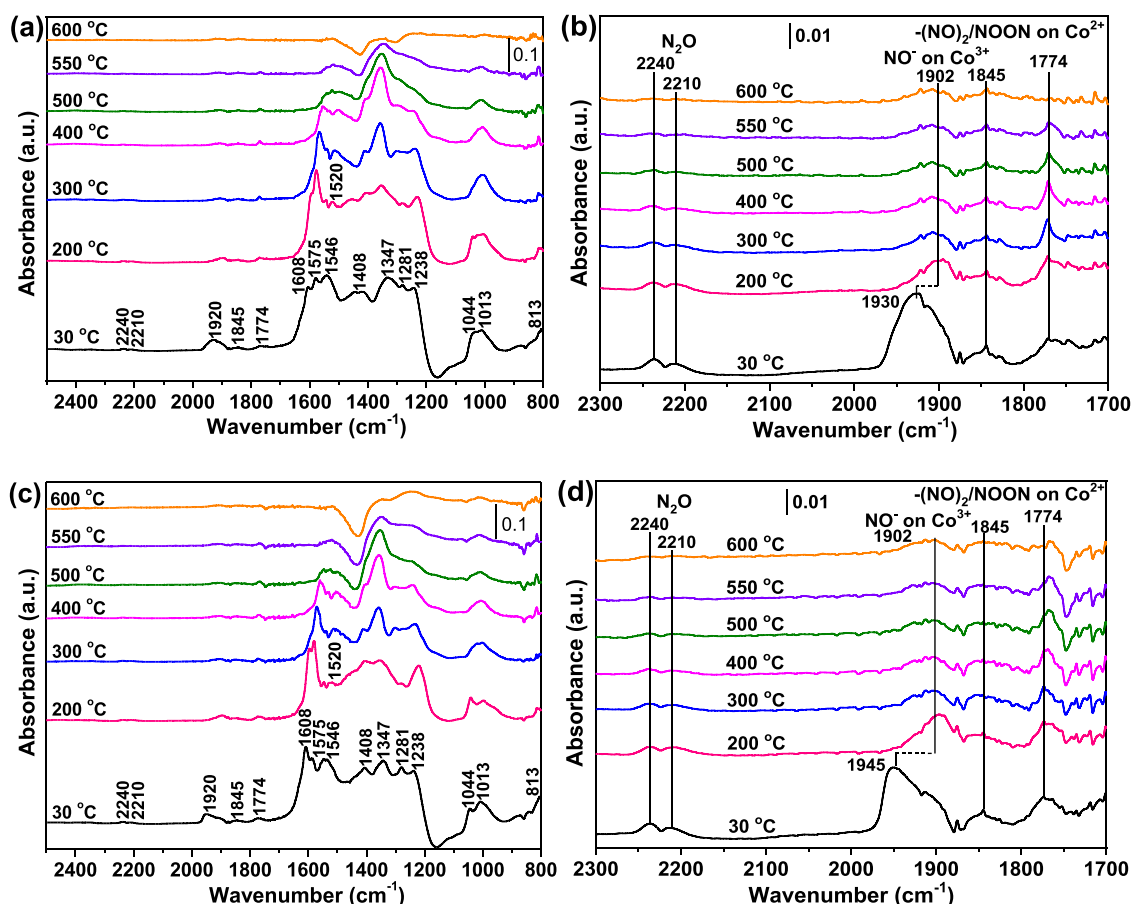


Fig. 7. *In situ* DRIFT profiles of BCR under (a), (b) 1 vol% NO/He, and (c), (d) 1 vol% NO+2 vol% O₂/He at 30–600 °C.

transfer and oxygen vacancy at the BCR interface (Fig. 5). The BCR surface contains Co³⁺ and Co²⁺ ions with an electron configuration of $t_{2g}^4 e_g^2$ and $t_{2g}^5 e_g^2$, respectively [52]. The Co³⁺ possesses more unpaired electron than Co²⁺, resulting in a promoting affinity for nitrogen donors when the ratio of Co³⁺/Co²⁺ increase [52]. By comparing the PSI on BaCoO₃ and BaCoO₃/CeO₂, we can observe that BaCoO₃/CeO₂ exhibits a stronger adsorption ability to NO. Furthermore, the NO adsorption sites on BaCoO₃/CeO₂ allow for the direct formation of *NOON species without the energy barrier. This characteristic enhances the catalytic performance of BaCoO₃/CeO₂, attributed to the synergistic effects between BaCoO₃ and CeO₂. The CeO₂ promotes the stabilization of the adsorbed species, leading to stronger NO adsorption. The proximity of the adsorption sites facilitates the direct formation of *NOON species, which further enhances the catalytic activity of BaCoO₃/CeO₂. Another factor contribute to the stronger catalytic performance of BaCoO₃/CeO₂ (110) is the influence of oxygen vacancy (O-vacancy). The electrons left behind with more oxygen vacancy formation which reduces Ce⁴⁺ (²F) to Ce³⁺ (¹S) ions [53]. It is well known in DFT results that the O vacancy tends to be on the CeO₂ (110) surface (1.69 eV). On CeO₂ (111) surfaces, it is usually located at subsurface sites (1.83 eV). It is also consistent with the experimentally observed higher concentration of oxygen vacancies in BCR samples. Consequently, oxygen vacancies located on the surface are more prone to migrate to the BaCoO₃, enhancing the coordination effects and promoting catalyst activity. Therefore, compared to BaCoO₃/CeO₂ (111) for BCP, the combination of stronger NO adsorption and the presence of surface oxygen vacancies in BaCoO₃/CeO₂ (110) for BCS and BCR contribute to its superior catalytic performance, in agreement with the activity results. That highlight the importance of surface orientation and oxygen vacancy distribution in determining the catalytic properties of composite materials.

Electronic interactions always occur at solid-solid interfaces and are simply driven by the principles of the system energy minimization and the continuity of the electric potential in the solid phases [54–56]. The redox interaction effect (Co³⁺ + Ce³⁺ ↔ Co²⁺ + Ce⁴⁺) produces long-range charge transfer and thereby causes more oxygen vacancies under the stable electric field on the concomitant BCR interface, suggesting the high availability of reaction environment on BCR with rod-like CeO₂. The BCR active interface is likely formed via a bonding between Co species in BaCoO₃ and the surface defect sites on both perovskite and ceria (Ce³⁺–O_v) species. The similar results of interface effect between metal site and the morphology of CeO₂ supports for other catalytic reactions were also verified in the literatures [18,57–60]. To sum up, the construction of active interface on BCR improves PSI and activates electronic interactions, promoting reducibility, lattice oxygen mobility with more Oxygen vacancy and NO adsorption and boosting the catalytic performance in NO direct decomposition reaction.

4.2. Proposed reaction pathways

The active sites of Co species and oxygen vacancies on the interfaces in BCR were observed. Combined with *in situ* DRIFT, isotopic (¹⁸O₂) exchange and DFT results, the NO molecules are effectively adsorbed on the Co species, but a competitive adsorption between NO and O₂ occurs on the oxygen vacancies after introducing O₂, resulting in a decrease of catalytic activity with the increasing operation time, in agreement with the results presented in Fig. 1d. Ba is more likely to promote the reduction of Co ions and formation of oxygen vacancy for stable ABO₃ perovskite type catalyst. Therefore, the reaction mechanism of NO direct decomposition over BCR catalyst is proposed in Scheme 2. NO molecule initially adsorbs on the active sites of Co species to form the mononitrosyl (NO*), and then interacts with an adjacent NO* on [] of active

Table 2
Detailed assignment of NO adsorption bands by *in situ* DRIFT profiles.

Wavenumber (cm ⁻¹)	Bond	Vibration	Adsorbed species	Structure
2240, 2210	N-N	ν	N ₂ O	—
1930, 1902, 1845	N-O	ν_{as}	NO on Co ³⁺	
1774	-O = N	ν	Asymmetric nitric oxide dimer, -(NO) ₂ /NOON on Co ²⁺ sites	
1608, 1044	N = O	ν	Bridging bidentate nitrate, (NO ₃)	
1575, 1546	N = O	ν	Chelating bidentate nitrate, (NO ₃)	
1520	-O-N-O	ν	Monodentate nitrite (NO ₂) on Co ³⁺	
1408	N = O	ν	Monodentate nitrate, (M-NO ₃)	
1347	N-O	ν_{as}	Nitrate free ion	—
1281, 1013	N-O	ν_s	Monodentate nitrate, (M-NO ₃)	
1238, 813	NO ₂	ν_{as}	Chelating bidentate nitrite (NO ₂) on CeO ₂	

* ν represents the stretching vibration; ν_{as} represents the asymmetric stretching vibration; ν_s represents the symmetric stretching vibration; M represents metal sites.

sites over the active interface to produce NOON*, as discussed in literature [61]. The easy formation of NOON* decomposes into N₂O* and the dissociated *O atom fills an oxygen vacancy on the surface to form active oxygen ([O²⁻]) species, verified in the *in-situ* DRIFT and DFT results. The

high mobility of lattice oxygen promotes this process, which is evidenced by the O₂-TPD and XPS results. The suitable amounts of lattice oxygen and oxygen vacancies on the surface of catalyst is beneficial to both the formation and consumption of NO*. Then the intermediates of *N₂O is broken with reaction energies at 1.11 eV to produce N₂ and the *O atom fills the vacancy (Fig. 9b). The adjacent active *O atom to further form O₂. Therefore, the decomposition of N₂O* is likely the rate-determining step (RDS) in NO direct decomposition over BCR. In addition, the original lattice ¹⁶O is consumed and replaced with the formation of lattice ¹⁸O via occupying more [] of the catalyst after adding excess gaseous ¹⁸O₂ in the isotopic (¹⁸O₂) exchange experiment. Herein the competitive adsorption of NO and O₂ on the [] mainly occurs in this step. The formed N₂O* species quickly decomposes into N₂ and another adsorbed oxygen (O*). Finally, the adjacent adsorbed oxygen (O*) species combine to produce O₂ and release active sites, which is ready for next catalytic cycle. The production of ¹⁶O¹⁸O is well verified with the formation and reaction of new lattice ¹⁸O in the above-mentioned isotopic (¹⁸O₂) tracing results. In this reaction mechanism, not only Co species acted as main active sites, but also oxygen vacancies play an important role on the BCR active interface for NO decomposition. The intrinsic effect with O₂ for NO direct decomposition shows that the suitable amount of lattice oxygen promotes the nitrite species formation at the beginning of the reaction. However, excessive amount of O₂ occupies more oxygen vacancies and inhibits the NO* formation and transformation of NO* into N₂O* due to the competitive adsorption of NO and O₂ on the oxygen vacancies, impeding the NO direct decomposition. The mobility of lattice oxygen and timely desorption of O₂ over the catalyst are crucial to further improve the catalytic activity and tolerance of O₂. These results contribute to our understanding of the perovskite-support interaction and reaction mechanisms and energetics involved in the NO adsorption and reaction processes on BaCoO₃/CeO₂ systems, shedding light on the potential catalytic activity of these materials in NO-related reactions.

5. Conclusion

The distinct structure-activity relationships of the BaCoO₃/CeO₂ catalysts were investigated using CeO₂ with conventional small particle (p), sphere (s) and rod (r) morphologies. The NTN₂ at 800 °C decreases in the order of BCR (78.9 %) > BCS (75.9 %) > BCP (56.9 %) > BaCoO₃ (8.6 %). BCR also exhibits a high durability (maintain NO conversion ~60 %) in the presence of 5 vol% O₂ for 12 h. Such superior catalytic activity and O₂ tolerance of BCR are attributed to the strong PSI on the oxide phases interface. The CeO₂ rod enhances the sintering resistance with high surface area, redox activity, mobility of active lattice oxygen and NO adsorption capability. We proposed a reaction mechanism that

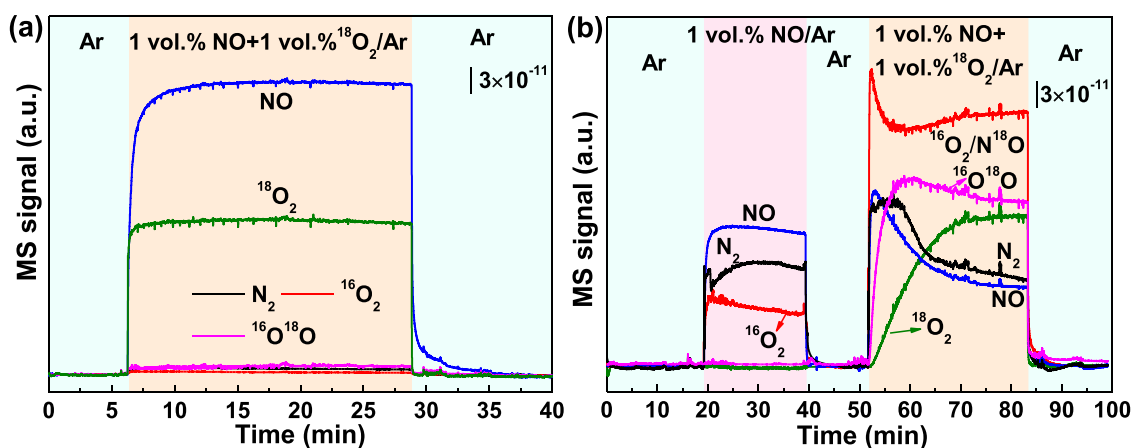


Fig. 8. Isotopic (¹⁸O₂) exchange experiments (a) blank calibration without catalyst at room temperature, and (b) NO direct decomposition processes at 800 °C over BCR at 1 vol% NO/Ar and 1 vol% NO + 1 vol% ¹⁸O₂/Ar conditions.

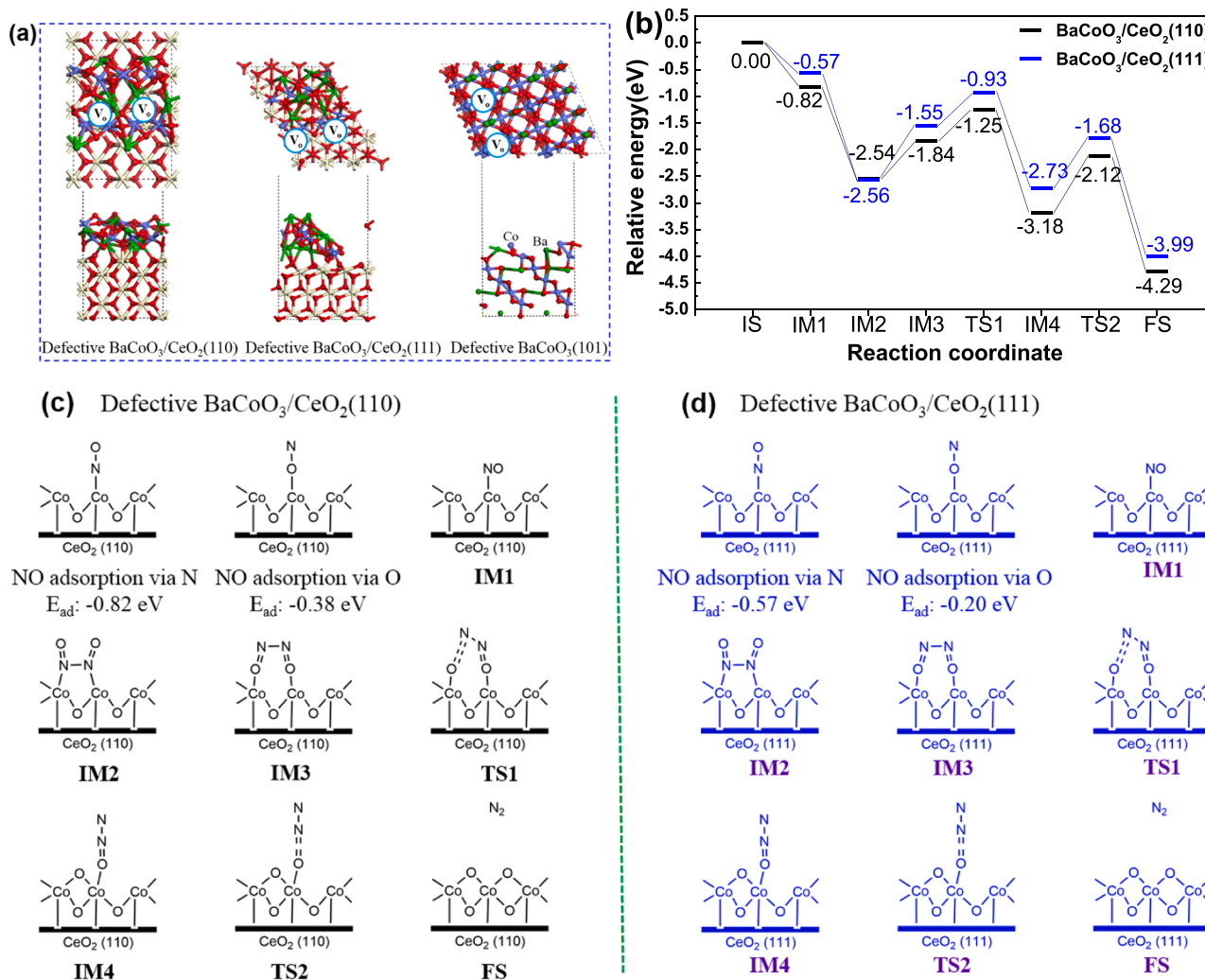
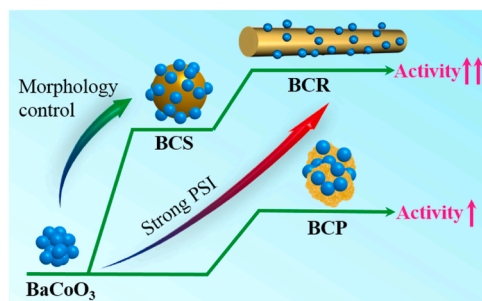
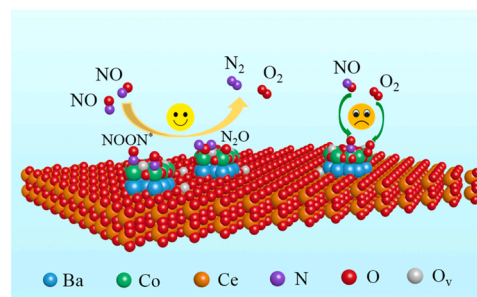


Fig. 9. (a) Optimized structure, (b) Energy profile and (c), (d) Reaction structure of NO direct decomposition.



Scheme 1. The morphology-activity relationship of catalysts.

both Co species and adjacent oxygen vacancies act as active sites, and the decomposition of N₂O* intermediate is the RDS. Further based on the isotopic (¹⁸O₂) exchange results, the intrinsic effect of adding O₂ highlights that an appropriate amount of lattice oxygen promotes the formation of nitrite species at the initial stage of the reaction. Nevertheless, an excessive amount of O₂ occupies more oxygen vacancies and thus inhibits the NO* formation and transformation of NO* into N₂O*, due to the competitive adsorption of NO and O₂ on the oxygen vacancies of active sites, inhibiting the NO direct decomposition reaction.



Scheme 2. Reaction pathways for NO direct decomposition over BCR catalyst.

CRediT authorship contribution statement

Lu Wang: Writing – original draft, Methodology, Investigation. **Gang Wang:** Supervision, Funding acquisition. **Hong Chen:** Validation, Methodology, Investigation. **Cuijuan Zhang:** Validation, Resources, Investigation. **Running Kang:** Writing – original draft, Methodology, Investigation, Formal analysis, Data curation, Conceptualization. **Xuehai Wang:** Writing – review & editing, Resources, Project administration. **Junqin Huang:** Investigation, Data curation. **Sufeng An:** Resources, Investigation, Conceptualization. **Feng Bin:** Validation, Resources, Investigation, Data curation. **Yongdan Li:** Writing – review &

editing, Supervision, Resources, Funding acquisition, Conceptualization.

Declaration of Competing Interest

The authors declare that they have no known competing financial interests or personal relationships that could have appeared to influence the work reported in this paper.

Data availability

No data was used for the research described in the article.

Acknowledgments

The authors gratefully acknowledge the financial support from the International Science and Technology Cooperation Projects (Sinopec. 410920). Running Kang sincerely acknowledge the financial support from the China Scholarship Council (CSC, No. 202004910623), China National Postdoctoral Program for Innovative Talents (No. BX20230380) and The Youth Fund of the State Key Laboratory of High Temperature Gas Dynamics (No.2023QN07). We also sincerely thank for the help of Gen Li (PhD student, DFT calculation and discussion, CSC No. 202208320030), Qianyu Qiu (PhD student, SEM operation, CSC No. 201906150134) and Penghui Yao (PhD student, catalyst preparation, CSC No. 202006120046), and DFT simulation from CSC-IT Center for Science, Finland, for computational resources.

Appendix A. Supporting information

Supplementary data associated with this article can be found in the online version at doi:10.1016/j.apcatb.2024.123952.

References

- [1] A. Tourunen, J. Saastamoinen, H. Nevalainen, Experimental trends of NO in circulating fluidized bed combustion, *Fuel* 88 (2009) 1333–1341.
- [2] R. Kang, J. He, F. Bin, B. Dou, Q. Hao, X. Wei, K. Hui, K.S. Hui, Alkali metal-resistant mechanism for selective catalytic reduction of nitric oxide over V_2O_5 /HWO catalysts, *Fuel* 304 (2021) 121445.
- [3] H. Zhao, X. Chen, A. Bhat, Y. Li, J.W. Schwank, Understanding the chemistry during the preparation of Pd/SSZ-13 for the low-temperature NO adsorption: the role of NH₄-SSZ-13 support, *Appl. Catal. B: Environ.* 282 (2017) 119611.
- [4] Y. Wu, X. Zhou, T. Mi, B. Hu, J. Liu, Q. Lu, Effect of WO₃ and MoO₃ doping on the interaction mechanism between arsenic oxide and V₂O₅-based SCR catalyst: a theoretical account, *Mol. Catal.* 499 (2021) 111317.
- [5] Y. Yang, J. Liu, F. Liu, Z. Wang, J. Ding, H. Huang, Reaction mechanism for NH₃-SCR of NO_x over CuMn₂O₄ catalyst, *Chem. Eng. J.* 316 (2019) 578–587.
- [6] D.D. Chen, Y.L. Yan, A.Q. Guo, V. Rizzotto, H.R. Lei, Z.W. Qiao, H. Liang, M. Jabloniska, X.Q. Jiang, J.X. Jiang, R. Palkovits, P.R. Chen, D.Q. Ye, U. Simon, Mechanistic insights into the promotion of low-temperature NH₃-SCR catalysis by copper auto-reduction in Cu-zeolites, *Appl. Catal. B: Environ.* 322 (2023) 122118.
- [7] J. Wang, H. Zhao, G. Haller, Y. Li, Recent advances in the selective catalytic reduction of NO_x with NH₃ on Cu-Chabazite catalysts, *Appl. Catal. B: Environ.* 202 (2021) 346–354.
- [8] J.J. Liu, X.Y. Shi, Y.B. Yu, M.Y. Zhang, D.R. Liu, H. He, Excellent hydrocarbon tolerance of CeO₂-WO₃-SnO₂ oxide catalyst for the NH₃-SCR of NO_x, *Appl. Catal. B: Environ.* 324 (2023) 122283.
- [9] Y. Zhang, G. Cao, X. Yang, Advances in De-NO_x methods and catalysts for direct catalytic decomposition of NO: a review, *Energy Fuels* 35 (2021) 6443–6464.
- [10] F. Garin, Mechanism of NO_x decomposition, *Appl. Catal. A Gen.* 222 (2001) 183–219.
- [11] P. Xie, W.X. Ji, Y. Li, C. Zhang, NO direct decomposition: progress, challenges and opportunities, *Catal. Sci. Technol.* 11 (2021) 374–391.
- [12] R.N. Kang, S.F. An, X.H. Wang, G. Wang, H. Chen, C.J. Zhang, F. Bin, Y.D. Li, Support effect and reaction pathway for NO direct decomposition over CuMn/A (A=ZSM-5, Beta, SSZ-13) catalysts, *Catal. Today* 430 (2024) 114545.
- [13] W.B. Bae, D.Y. Kim, S.W. Byun, S.J. Lee, S.K. Kuk, H.J. Kwon, H.C. Lee, M. J. Hazlett, C. Liu, Y.J. Kim, M. Kim, S.B. Kang, Direct NO decomposition over Rh-supported catalysts for exhaust emission control, *Chem. Eng. J.* 475 (2023) 146005.
- [14] M.S. Jia, R.J. Deng, F. Li, K.W. Xu, Y. Ye, Z.F. Wang, H.L. Yang, X.H. Wang, Solution combustion synthesis of a Y_{0.87}Ba_{0.1}Zr_{0.03}O_{1.465} catalyst for highly efficient NO direct decomposition at high temperatures, *Energy Fuels* 37 (2023) 19704–19714.
- [15] S. Royer, D. Duprez, F. Can, X. Courtois, C. Batiot-Dupeyrat, S. Laassiri, H. Alamdari, Perovskites as substitutes of noble metals for heterogeneous catalysis: dream or reality, *Chem. Rev.* 114 (2014) 10292–10368.
- [16] W. Xu, J. Cai, J. Zhou, Y. Ou, W. Long, Z. You, Y. Luo, Highly effective direct decomposition of nitric oxide by microwave catalysis over BaMeO₃ (Me=Mn, Co, Fe) mixed oxides at low temperature under excess oxygen, *ChemCatChem* 8 (2016) 417–425.
- [17] M. Jang, S. Yoon, D. Shin, H. Kim, R. Huang, E. Yang, J.H. Kim, K.S. Lee, K. An, J. W. Han, Boosting, support reducibility and metal dispersion by exposed surface atom control for highly active supported metal catalysts, *ACS Catal.* 12 (2022) 4402–4414.
- [18] Y. Gao, Z. Zhang, Z. Li, W. Huang, Understanding morphology-dependent CuO_x-CeO₂ interactions from the very beginning, *Chin. J. Catal.* 41 (2020) 1006–1016.
- [19] P. Xie, X. Yong, M. Wei, Y. Li, C. Zhang, High performance catalysts BaCoO₃-CeO₂ prepared by the one-pot method for NO direct decomposition, *ChemCatChem* 12 (2020) 4297–4303.
- [20] P. Xie, X. Yong, Y. Li, S. Liu, C. Zhang, Tailoring the BaCoO₃-CeO₂ catalyst for NO direct decomposition: Factors determining catalytic activity, *J. Catal.* 400 (2021) 301–309.
- [21] W. Ji, P. Xie, Y. Li, C. Zhang, Highly efficient NO direct decomposition over BaMnO₃-CeO₂ composite catalysts, *Appl. Catal. A Gen.* 634 (2022) 118543.
- [22] S. Shin, H. Arakawa, Y. Hatakeyama, K. Ogawa, K. Shimomura, Absorption of NO in the lattice of an oxygen-deficient perovskite SrFeO_{3-x} and the infrared spectroscopic study of the system NO-SrFeO_{3-x}, *Mater. Res. Bull.* 14 (1979) 633–639.
- [23] Y. Teraoka, T. Harada, S. Kagawa, Reaction mechanism of direct decomposition of nitric oxide over Co- and Mn-based perovskite-type oxides, *J. Chem. Soc. Faraday Trans. 94* (1998) 1887–1891.
- [24] L. Chen, X. Niu, Z. Li, Y. Dong, D. Wang, F. Yuan, Y. Zhu, The effects of BaO on the catalytic activity of La_{1.6}Ba_{0.4}NiO₄ in direct decomposition of NO, *J. M. Catal. A: Chem.* 423 (2016) 277–284.
- [25] H. Iwakuni, Y. Shinmyou, H. Yano, H. Matsumoto, T. Ishihara, Direct decomposition of NO into N₂ and O₂ on BaMnO₃-based perovskite oxides, *Appl. Catal. B: Environ.* 74 (2007) 299–306.
- [26] S. Fang, A. Takagaki, M. Watanabe, T. Ishihara, The direct decomposition of NO into N₂ and O₂ over copper doped Ba₃Y₄O₉, *Catal. Sci. Technol.* 10 (2020) 2513–2522.
- [27] S. Tsujimoto, K. Yasuda, T. Masui, N. Imanaka, Effects of Tb and Ba introduction on the reaction mechanism of direct NO decomposition over C-type cubic rare earth oxides based on Y₂O₃, *Catal. Sci. Technol.* 3 (2013) 1928–1936.
- [28] P. Sudarsanam, B. Hillary, B. Mallesham, B.G. Rao, M.H. Amin, A. Nafady, A. M. Alsalmeh, B.M. Reddy, S.K. Bhargava, Designing CuO_x nanoparticle-decorated CeO₂ nanocubes for catalytic soot oxidation: role of the nanointerface in the catalytic performance of heterostructured nanomaterials, *Langmuir* 32 (2016) 2208–2215.
- [29] Y. Guo, Y. Qin, H. Liu, H. Wang, J. Han, X. Zhu, Q. Ge, CeO₂ facet-dependent surface reactive intermediates and activity during ketonization of propionic acid, *ACS Catal.* 12 (2022) 2998–3012.
- [30] G.K. Reddy, T.C. Peck, C.A. Roberts, CeO₂-M_xO_y (M = Fe, Co, Ni, and Cu)-based oxides for direct NO decomposition, *J. Phys. Chem. C* 123 (2019) 28695–28706.
- [31] J. Ma, G. Jin, J. Gao, Y. Li, L. Dong, M. Huang, Q. Huang, B. Li, Catalytic effect of two-phase intergrowth and coexistence CuO-CeO₂, *J. Mater. Chem. A* 3 (2015) 24358–24370.
- [32] R. Kang, P. Ma, J. He, H. Li, F. Bin, X. Wei, B. Dou, K.N. Hui, K.S. Hui, Transient, behavior and reaction mechanism of CO catalytic ignition over a CuO-CeO₂ mixed oxide, *Proc. Combust. Inst.* 38 (2021) 6493–6501.
- [33] X. Liao, W. Chu, X. Dai, V. Pitchon, Promoting effect of Fe in preferential oxidation of carbon monoxide reaction (PROX) on Au/CeO₂, *Appl. Catal. A Gen.* 449 (2012) 131–138.
- [34] W. Zhao, X. Zheng, S. Liang, X. Zheng, L. Shen, F. Liu, Y. Cao, Z. Wei, L. Jiang, Fe-doped γ-Al₂O₃ porous hollow microspheres for enhanced oxidative desulfurization: facile fabrication and reaction mechanism, *Green Chem.* 20 (2018) 4645–4654.
- [35] S. Liu, Y. Cong, C. Kappenstein, T. Zhang, Effect of zirconium in La(Ba)Zr_{1-x}Co_xO_{3-δ} perovskite catalysts for N₂O decomposition, *Chin. J. Catal.* 33 (2012) 907.
- [36] K. Chen, B. Chu, Q. Qin, X. Ou, R. Zhao, X. Wei, H. Wu, B. Li, L. Dong, Effect of reduction on NO + CO reaction performance of CuO-Co₃O₄ symbiotic oxide porous nanosheet and DFT calculation, *Appl. Surf. Sci.* 589 (2022) 153052.
- [37] H. Zhu, Z. Qin, W. Shan, W. Shen, J. Wang, Pd/CeO₂-TiO₂ catalyst for CO oxidation at low temperature: a TPR study with H₂ and CO as reducing agents, *J. Catal.* 255 (2004) 267–277.
- [38] Z. Zhao, X. Yang, Y. Wu, Comparative study of Nickel-based perovskite-like mixed oxide catalysts for direct decomposition of NO, *Appl. Catal. B: Environ.* 8 (1996) 281–297.
- [39] G.K. Reddy, T.C. Peck, C.A. Roberts, CeO₂-M_xO_y (M = Fe, Co, Ni, and Cu)-based oxides for direct NO decomposition, *J. Phys. Chem. C* 123 (2019) 28695.
- [40] J. Chen, M. Shen, X. Wang, J. Wang, Y. Su, Z. Zhao, Catalytic performance of NO oxidation over LaMeO₃ (Me = Mn, Fe, Co) perovskite prepared by the sol–gel method, *Catal. Commun.* 37 (2013) 105–108.
- [41] T. Ishihara, M. Ando, K. Sada, K. Takiishi, K. Yamada, H. Nishiguchi, Y. Takita, Direct decomposition of NO into N₂ and O₂ over La(Ba)Mn(In)O₃ perovskite oxide, *J. Catal.* 220 (2003) 104–114.
- [42] Y. Li, T.L. Slager, J.N. Armor, Selective reduction of NO_x by methane on Co-Ferrierites: II. Catalyst characterization, *J. Catal.* 150 (1994) 388–399.
- [43] K. Hadjiivanov, B. Tsyntsrskii, T. Nikolova, Stability and reactivity of the nitrogen-oxo species formed after NO adsorption and NO+O₂ coadsorption on Co-ZSM-5: an FTIR spectroscopic study, *Phys. Chem. Chem. Phys.* 1 (1999) 4521–4528.

- [44] K.A. Windhorst, J.H. Lunsford, Structure and reactivity of cobalt-nitrosyl complexes in Y-type zeolites, *J. Am. Chem. Soc.* 97 (1975) 1407–1412.
- [45] B. Djonev, B. Tsyntsarski, D. Klissurski, K. Hadjiivanov, IR spectroscopic study of NO_x adsorption and NO_x-O₂ coadsorption on Co²⁺/SiO₂ catalysts, *J. Chem. Soc. Faraday Trans.* 93 (1997) 4055–4063.
- [46] A. Martínez-Arias, J. Soria, J.C. Conesa, X.L. Seoane, A. Arcoya, R. Cataluña, NO reaction at surface oxygen vacancies generated in cerium oxide, *J. Chem. Soc. Faraday Trans.* 91 (1995) 1679–1687.
- [47] D. Pozdnyakov, V. Filimonov, Infrared spectroscopic study of the chemisorption of nitric oxide and nitrogen dioxide on metal oxides, *Kinet. Katal.* 14 (1973) 760–766.
- [48] S. Xie, M.P. Rosynek, J.H. Lunsford, Catalytic reactions of NO over 0–7 mol % Ba/MgO catalysts: I. the direct decomposition of NO, *J. Catal.* 188 (1999) 24–31.
- [49] J.S.J. Hargreaves, S.D. Jackson, G. Webb, *Isotopes on Heterogeneous catalysis. Catalytic Science Series*, 4.
- [50] Z. Pan, Y. Li, Y. Zhao, C. Zhang, H. Chen, Bulk phase charge transfer in focus – and in sequential along with surface steps, *Catal. Today* 364 (2021) 2–6.
- [51] D. Damma, T. Boningari, P.R. Ettireddy, B.M. Reddy, P.G. Smirnotis, Direct decomposition of NO_x over TiO₂ supported transition metal oxides at low temperatures, *Ind. Eng. Chem. Res.* 57 (2018) 16615–16621.
- [52] J. Ndalamo, A.F. Mulaba-Bafubandi, B.B. Mamba, UV/visible spectroscopic analysis of Co³⁺ and Co²⁺ during the dissolution of cobalt from mixed Co-Cu oxidized ores, *Int. J. Miner. Metall. Mater.* 18 (2010) 260–269.
- [53] J.D. Cafun, K.O. Kvashnina, E. Casals, V.F. Puentes, P. Glatzel, Absence of Ce³⁺ sites in chemically active colloidal ceria nanoparticles, *ACS Nano* 7 (2013) 10726–10732.
- [54] R.T. Tung, Recent advances in Schottky barrier concepts, *Mater. Sci. Eng. R.* 35 (2001) 1–138.
- [55] J. Wang, T. Fu, F. Meng, D. Zhao, S.S.C. Chuang, Z. Li, Highly active catalysis of methanol oxidative carbonylation over nano Cu₂O supported on micropore-rich mesoporous carbon, *Appl. Catal. B: Environ.* 303 (2022) 120890.
- [56] R.N. Kang, J.Q. Huang, F. Bin, Z.H. Teng, X.L. Wei, B.J. Dou, S. Kasipandi, Evolution behavior and active oxygen quantification of reaction mechanism on cube Cu₂O for CO self-sustained catalytic combustion and chemical-looping combustion, *Appl. Catal. B: Environ.* 310 (2022) 121296.
- [57] A. Chen, X. Yu, Y. Zhou, S. Miao, Y. Li, S. Kuld, J. Sehested, J. Liu, T. Aoki, S. Hong, M.F. Camellone, S. Fabris, J. Ning, C. Jin, C. Yang, A. Nefedov, C. Wöll, Y. Wang, W. Shen, Structure of the catalytically active copper–ceria interfacial perimeter, *Nat. Catal.* 2 (2019) 334–341.
- [58] S.D. Senanayake, D. Stacchiola, J.A. Rodriguez, Unique properties of ceria nanoparticles supported on metals: novel inverse ceria/copper catalysts for CO oxidation and the water–gas shift reaction, *Acc. Chem. Res.* 46 (2013) 1702–1711.
- [59] T.E. James, S.L. Hemmingson, C.T. Campbell, Energy of supported metal catalysts: from single atoms to large metal nanoparticles, *ACS Catal.* 5 (2015) 5673–5678.
- [60] X.H. Zheng, Y.L. Li, L.Y. Zhang, L.J. Shen, Y.H. Xiao, Y.F. Zhang, C. Au, L.L. Jiang, Insight into the effect of morphology on catalytic performance of porous CeO₂ nanocrystals for H₂S selective oxidation, *Appl. Catal. B: Environ.* 252 (2019) 98–110.
- [61] M. Haneda, Y. Kintaichi, H. Hamada, Reaction mechanism of NO decomposition over alkali metal-doped cobalt oxide catalysts, *Appl. Catal. B: Environ.* 55 (2005) 169–175.